Available online at www.sciencedirect.com
ScienceDirect
Trans. Nonferrous Met. Soc. China 32(2022) 2620−2633

Transactions of Nonferrous Metals Society of China
www.tnmsc.cn

Improving oxidation resistance of porous FeAl-based intermetallics with high boron/yttrium alloying

Hui-bin ZHANG, Hang YU, Jun-liang MA, Long-fei WANG, Sheng-hang XU, Guo-qu ZHENG

College of Materials Science and Engineering, Zhejiang University of Technology, Hangzhou 310014, China

Received 2 August 2021; accepted 29 December 2021

Abstract: The coalloying with high contents of chromium (Cr), boron (B) and yttrium (Y) for porous *B*2-structured FeAl intermetallics fabricated through reactive synthesis was conducted. The oxidation behaviors of porous FeAl-based materials were investigated by evaluating the pore-structure evolution, oxidation kinetics and oxide-scale configuration. The results show that with the coalloying of high contents of Cr, B and Y, the oxidation mass gains of porous FeAl materials at 600−800 °C are significantly reduced. The combination of B enriched on the surface of oxide scales and Y located at the scale−metal interface promotes the formation of thin protective nodular α-Al_2O_3 oxide scales. It is indicated that introducing relatively high contents of reactive elements such as B and Y can benefit the selective growth of α-Al_2O_3 scales at relatively low temperatures without pre-treatment.

Key words: FeAl; intermetallics; yttrium; high-temperature filter material; oxidation; porous material

---

1 Introduction

High-temperature filtration has been widely used in steel, coal chemical, petrochemical, and thermal power industries since it can better meet the requirements of waste heat recovery, high-temperature selective catalytic reduction (SCR) of nitrous oxides, and avoiding liquid-phase condensation [1,2]. The filter material is the key component in any elevated-temperature filtration. In addition to the finer pore structure and lower filtration resistance, filter material selection and development have been pursuing the increased strength and better corrosion resistance to cope with hotter processes, thus improving filtration performance and life-cycle costs [1]. Iron−aluminium (FeAl) intermetallic is a special alloy with the merits of low material cost, excellent structural strength, and outstanding resistance to the corrosive and erosive gas environment [3,4]. Therefore, FeAl has been introduced into the high-temperature filter material family in recent years [3−6].

Binary Fe−Al intermetallics were firstly developed into filter materials, and common FeAl alloys are Fe_3Al (22.5−33 at.% Al) and *B*2-structured FeAl (33−51 at.% Al) [7]. Binary Fe−Al porous materials can form protective Al_2O_3 scales against high-temperature oxidation. The Al_2O_3 formed at different temperatures with different durations has different polymorphs, including metastable θ-Al_2O_3 and γ-Al_2O_3, as well as low defect α-Al_2O_3, among which the hexagonal α-Al_2O_3 shows the lowest growth rate due to its minimum defect mobility [8,9]. However, at common service temperatures of 600−800 °C, the defective metastable γ/θ-Al_2O_3 is always mingled in the oxide scales of porous FeAl [10]. Based on the binary FeAl, the addition of Cr can produce the so-called "third-element effect" [9,11], which can decrease the critical Al content to form Al_2O_3 scales. Cr alloying can also remarkably improve the ductility and strength of FeAl filter material at the

---

Corresponding author: Hui-bin ZHANG, Tel: +86-573-88320429, E-mail: zhanghb@zjut.edu.cn

DOI: 10.1016/S1003-6326(22)65971-5

ambient and elevated temperatures [12]. Therefore, FeAlCr filter material with the improved resistances to corrosion and heat can be applied at temperatures above 700 °C. In addition, boron (B) and yttrium (Y) are common alloying elements in FeCrAl alloys and their roles in modifying the mechanical properties and anticorrosion performance of FeCrAl alloys have been well confirmed [13−15].

Up to now, great effort has been made to investigate the oxidation behaviors of dense FeAl-based alloys developed for high-temperature structural materials [8,11,16,17]. Traditional alloy design for structural materials is more concerned on the mechanical property, while as for porous materials with high surface areas and interconnected open-pore structures, the alloying strategy should be more focused on the ability to form the thin protective oxide scales. Oxidation is the most extensive corrosion that possibly degrades the mechanical performance and permeability of porous metals. The sulfidation of metal materials is sometimes more rapid than oxidation, but the oxide scale formed under the mixed gas atmosphere is still one of the primary mechanisms protecting material against sulfidation corrosion [18]. Therefore, a detailed knowledge of the oxidation behaviors of FeAl-based filter materials is essential for the reliable prediction of the material application.

It is well known that *B*2-structured FeAl phase has relatively high solubility for various alloying elements [7]. Thus, improving the oxidation performance of porous FeAl is expected to be realized by special alloying. The self-healing properties as well as the service life of porous materials also depend on the reserve of reactive elements [19]. That is to say, the high-alloying strategy may serve better for porous FeAl. Regarding the possible benefits of reactive elements Cr, B, and Y, in this work, a series of FeAl-based porous materials (FeAl, FeAlCr, FeAlCrB, and FeAlCrBY) were prepared and their oxidation behaviors were investigated. Especial attention was paid to the roles of relatively high contents of B and Y in the oxidation behaviors of porous FeAl-based materials.

2 Experimental

2.1 Materials and synthesis

The elemental powders of Fe (mean particle size of 40 μm, purity >99.5%), Al (mean particle size of 40 μm, purity >99.5%), Cr (mean particle size of 8.0 μm, purity >99.5%), B (particle size of 1.0−3.0 μm, purity >99.99%) and Y (mean particle size of 1.0 μm, purity >99.5%) were used as raw materials. The raw powders were put into the V-type mixer after being weighed according to the assigned proportions (Fe−25Al, Fe−22.5Al−10Cr, Fe−22.5Al−10Cr−0.2B, Fe−22.5Al−10Cr−0.2B−0.2Y, wt.%). Zirconia balls were added to the raw powders to enhance the mixing efficiency and obtain uniform mixtures. Each batch of powders was blended for 12 h and then mixed with 2.0 wt.% octadecanoic acid using ethanol as solvent. After drying and second shattering with 40 mesh sieves, the pelletized coarse particles were formed into sheet compact (*d*20 mm × 2.0 mm) by mold pressing under a pressure of 200 MPa. A step-sintering schedule was used to conduct the reactive synthesis of green compacts in a vacuum sintering furnace with a vacuum degree lower than 1.0×10^{-2} Pa. The holding temperatures were respectively 150, 450, 600, and 1250 °C to remove the adsorbed gas molecules, pyrolyze the binder, and assure the complete inter-diffusion of elements and well-grown porous skeletons. The synthesized porous materials were obtained after cooling in the furnace.

2.2 Oxidation tests

Constant-temperature oxidation experiments were carried out according to HB 5258—2000, a method for determination of oxidation resistance of steels and superalloys, and the samples burned to constant mass in advance were placed in a quartz crucible. Samples were kept in line or point contact with the crucible to ensure that the sample could fully contact with air. The oxidation was carried out in a muffle furnace (temperature accuracy ±5 °C) at 600−800 °C. The samples were taken out and weighed at regular intervals to obtain the oxidation mass gain curves. The total time of oxidation was 100 h, and the resolution of the analytical balance was 1.0×10^{-7} kg.

2.3 Characterization

Microstructures and compositions of the prepared and oxidized samples were observed using SEM (Zeiss Merlin, operated at 20 kV) equipped with energy dispersion spectroscopy (EDS). The cross-section view was prepared in an epoxy mount and polished before SEM and BSE observation. The phase composition was investigated using X-ray diffraction (XRD, RIGAKU D/Max 2550 PC, Cu K_α, 40 kV, 40 mA, scanning rate 5 (°)/min). The bubble point method was used to measure the pore size of porous materials [20]. Porosity was determined by the Archimedes method as specified in the ASTM B962–08 standard. X-ray photoelectron spectroscopy (XPS) was tested with Thermo Fisher Scientific ESCALAB 250Xi (Al K_α X-ray source, $h\nu$=1486.6 eV).

3 Results and discussion

3.1 Characterization of synthesized materials

Figure 1 presents the XRD patterns of the four synthesized porous materials. After high-temperature sintering, all groups of FeAl-based porous materials alloyed with Cr, Cr/B, and Cr/B/Y have the characteristic of a single FeAl phase with a *B*2 structure (PDF #33-0020, primitive cubic, space group $Pm\bar{3}m$) [21]. No minor phases or elemental metals (Cr or Y) are detected, indicating that the alloying elements have been well dissolved in FeAl phase. The differences in atomic radii of Fe (0.124 nm), Cr (0.125 nm), Al (0.143 nm), B (0.095 nm), and Y (0.227 nm) can explain the deviations of the (110) peak of these Fe−Al materials. As shown in Fig. 1, the solid solution of 10 wt.% Cr leads to the left shift of diffraction peak position. Cr atoms with a bigger atomic radius mainly occupy the positions of Fe atoms, leading to increased pacing of crystal. The main peaks of the sintered FeAlCrB are slightly shifted to the direction of the high angle due to the substitution of Al/Fe vacancies by B atoms with the smallest atomic radius [13]. As for FeAlCrBY, the addition of Y with the largest atomic radius slightly neutralizes the rightward shift of the (110) peak caused by B alloying.

Figure 2 shows the cross-section and surface morphologies of porous FeAl, FeAlCr, FeAlCrB, and FeAlCrBY intermetallics. The well-developed sintering necks and porous structures are obtained in all samples. Compared with the sintered metal porous materials using pre-alloyed powders [6], these reactively synthesized porous materials possess mellow skeletons and abundant porosities. A partial pore volume generated by partial diffusion and phase transformation improves the connection among the powder−interstitial pores, making the synthesized materials have a smaller tortuosity factor, thus helping to reduce the filtration pressure when applied in gas−solid filtration. With the successive addition of Cr, B, and Y, it has been shown that the pore size and porosity of FeAl-based porous materials are increased. To be specific, the mean pore size of FeAl-based porous materials increases from 28.95 to 40.38 μm, and the porosity rises from 35.17% to 49.87% (Table 1). The addition of Cr to the Fe−Al binary system aggravates the volume expansion due to the significant orientation growth of the Al_4Cr phase formed by diffusion reaction between Al and Cr [21]. The growth of intermetallic compound phases among compacted powders can promote the connectivity of the initial interstitial pores, Kirkendall pores, and phase-change pores [22], thus increasing the porosity and equivalent pore size. The enlarged porosities and pore sizes of porous FeAlCrB and FeAlCrBY materials are probably attributed to the growth of neonatal intermediate intermetallic phases at temperatures around the melting point of Al, which has been revealed in the Fe−Al−Si system [4,5].

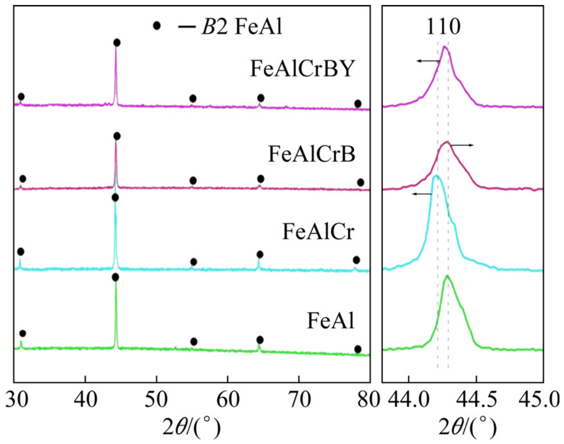

Fig. 1 XRD patterns of synthesized porous FeAl, FeAlCr, FeAlCrB, and FeAlCrBY materials

3.2 Oxidation kinetics

Figure 3 reveals the cyclic oxidation kinetics of the synthesized porous materials. Figure 3(a) shows that, after 100 h of oxidation, the oxidation mass gain of porous FeAl increases from 0.75 to 3.50 wt.% with the temperature increasing from 600 to 800 °C. With the addition of ternary element Cr,

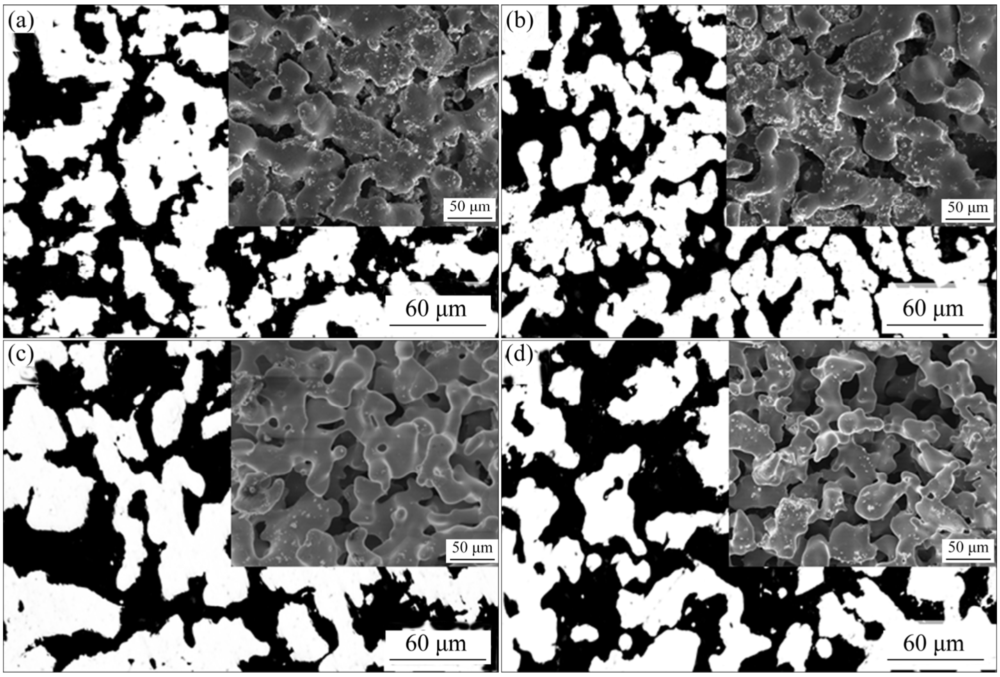

Fig. 2 Sectional-view and surface morphological (insets) images of porous FeAl (a), FeAlCr (b), FeAlCrB (c), and FeAlCrBY (d) materials

Table 1 Pore parameters of porous FeAl, FeAlCr, FeAlCrB, and FeAlCrBY materials

Material	Mean pore size/μm	Open porosity/%
FeAl	28.95	35.17
FeAlCr	33.68	38.51
FeAlCrB	35.75	44.94
FeAlCrBY	40.38	49.87

the mass gains of porous FeAlCr at 600, 700, and 800 °C reduce to 0.19, 0.25, and 1.50 wt.%, respectively, which are much lower than those of porous FeAl (Fig. 3(b)). This indicates that the "third element effect" [23] of Cr on the oxidation resistance of FeAl is quite arresting. The oxidation mass gains of porous FeAlCrB are comparable to those of porous FeAlCr at 600 and 700 °C (Fig. 3(c)), but less than those of porous FeAlCr at 800 °C (0.99 wt.%), indicating that B alloying modifies the oxidation resistance of porous FeAlCr at 800 °C. As shown in Fig. 3(d), porous FeAlCrBY gains the minimum mass increments at 600−800 °C among the four materials. Particularly, the mass gain of porous FeAlCrBY is 0.39 wt.% after 100 h of oxidation at 800 °C, only 26% that of porous FeAlCr, indicating that the coalloying of B and Y based on FeAlCr is beneficial to the antioxidant property. Besides, it is noted that the oxidation mass gains for porous FeAlCr and FeAlCrB at 800 °C increase drastically, implying that an abnormal oxidation takes place. Fortunately, the coalloying of B and Y can well suppress such rapid oxidation.

As shown in Fig. 3, the cyclic oxidation of these porous FeAl-based materials shows the characteristics of two stages. At the initial stage of oxidation with a time less than 30 h, the oxidation of these porous materials follows a parabolic rate law. A modified Wagner rate law [21] is used in the present case for porous material evaluation:

$$(\Delta m/m_0)^2=k_\mathrm{p}t \tag{1}$$

where Δm is the mass change after oxidation, m_0 is the initial mass of the sample, k_p is parabolic law constant, and t is the oxidation time. The parabolic-rate oxidation is related to the construction of the oxide film and the porous structure of porous materials, while a linear rate law indicates the generation of the intact oxide scales on the tested materials with the oxidation behaviors carried out in a stable diffusion-controlled stage [24]. The rate constants and determination coefficients for the data fitting of these two stages of these materials are listed in Table 2. Specifically, the oxidation rates of porous

FeAlCrBY at the stable stage become quite slow, indicating its excellent antioxidant performance during the stable oxidation period at 600−800 °C. Such oxidation resistivity of porous FeAl-based intermetallic compounds is much superior to that of other reported porous stainless steel [25] and Fe−Cr

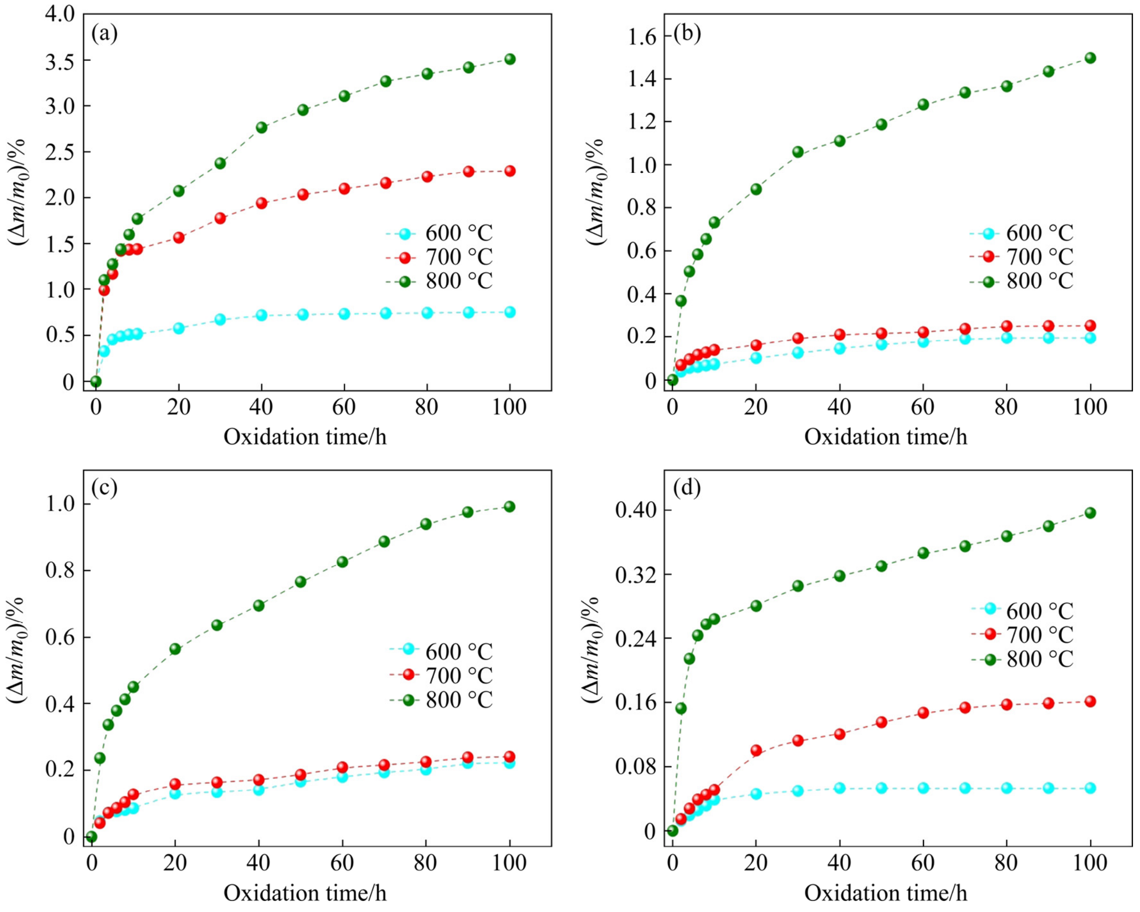

Fig. 3 Oxidation mass-gain curves of porous FeAl (a), FeAlCr (b), FeAlCrB (c), and FeAlCrBY (d) materials at 600, 700, and 800 °C for 100 h

Table 2 Rate constants of oxidation and determination of coefficients R^2 for initial (t<30 h) and subsequent stable oxidation stages of porous FeAl, FeAlCr, FeAlCrB, and FeAlCrBY materials

Sample	Initial oxidation stage		Stable oxidation stage	
	Parabolic rate constant, k_1/(%^{2}·h^{-1})	R^2	Linear rate constant, k_2/(%·h^{-1})	R^2
FeAl (600 °C)	1.4×10^{-4}	0.85	1.0×10^{-5}	0.73
FeAlCr (600 °C)	3.4×10^{-5}	0.87	1.3×10^{-5}	0.87
FeAlCrB (600 °C)	4.6×10^{-5}	0.98	1.2×10^{-5}	0.97
FeAlCrBY (600 °C)	2.4×10^{-5}	0.79	1.2×10^{-8}	0.93
FeAl (700 °C)	5.6×10^{-4}	0.90	8.5×10^{-5}	0.90
FeAlCr (700 °C)	4.1×10^{-5}	0.95	1.2×10^{-5}	0.89
FeAlCrB (700 °C)	5.4×10^{-5}	0.99	1.1×10^{-5}	0.97
FeAlCrBY (700 °C)	8.2×10^{-5}	0.91	7.9×10^{-6}	0.91
FeAl (800 °C)	3.6×10^{-2}	0.90	1.7×10^{-4}	0.91
FeAlCr (800 °C)	7.4×10^{-3}	0.84	7.1×10^{-5}	0.96
FeAlCrB (800 °C)	1.9×10^{-3}	0.89	5.6×10^{-5}	0.98
FeAlCrYB (800 °C)	3.2×10^{-4}	0.73	1.4×10^{-5}	0.99

alloys [26] (Table 3). The evolutions of parabolic rate constant (k_1) as a function of temperatures are depicted as the Arrhenius plot (Fig. 4). From the slopes of the linear fitting of the natural logarithm of k_1 as a function of $1/T$, the values of the apparent activation energies for each material can be calculated. As revealed by the three separate straight lines of alumina polymorphs in the Arrhenius diagram [10], the activation energy for the oxidation of porous FeAlCrBY is comparable to that of α-Al_2O_3, while that of porous FeAlCr and FeAlCrB is close to that of metastable Al_2O_3. The activation energy for the oxidation of porous FeAl is the lowest, suggesting that formed oxide scales provide poor protection against oxidation [11,17].

As shown in Fig. 3, Cr alloying provides very good oxidation protection for porous FeAl only at low temperatures of 600−700 °C. The role of chromium oxides in the formation of protective scales was reported in many researches [11,17]. Cr improves the oxidation resistance of FeAl alloys at low temperatures due to the formation of composite chromic oxides with Fe/Al oxides [27]. At high temperatures above 800 °C, the Cr_2O_3 transforms to volatilizable CrO_3 [23], which can be the reason of the enhanced oxidation occurring on porous FeAlCr and FeAlCrB at 800 °C (Figs. 3(b, c)). This also proves that at high temperatures the oxidation resistance mainly depends on the formability of stable aluminum oxide scales. It is noteworthy that coalloying of Cr, B, and Y reduces the oxidation mass gain of porous FeAl oxidized at 800 °C for 100 h from 3.5% to 0.39%, suggesting that the configuration of the protective oxide scales has been substantially ameliorated. Therefore, this work is focused on the radical improvement of the antioxidation property of porous FeAl with the coalloying of Cr, B, and Y at 800 °C.

Table 3 Comparison of parabolic rate constants of some porous materials tested by cyclic oxidation at different temperatures

Porous material	Temperature/°C	K/($\%^2\cdot h^{-1}$)	Porosity/%	Ref.
FeAl−5%Cr	600	3.59×10^{-5}	40.2−40.9	[21]
FeCrAl	600	5.89×10^{-5}	27−30	[6]
FeAlCrBY	600	2.41×10^{-5}	49−51	This work
316L	800	8.72×10^{-2}	−	[25]
FeCr	800	0.13	25−40	[26]
FeAl	800	3.60×10^{-2}	34−36	This work
FeAlCr	800	7.42×10^{-3}	36−39	This work
FeAlCrB	800	1.91×10^{-3}	44−46	This work
FeAlCrBY	800	3.22×10^{-4}	49−51	This work

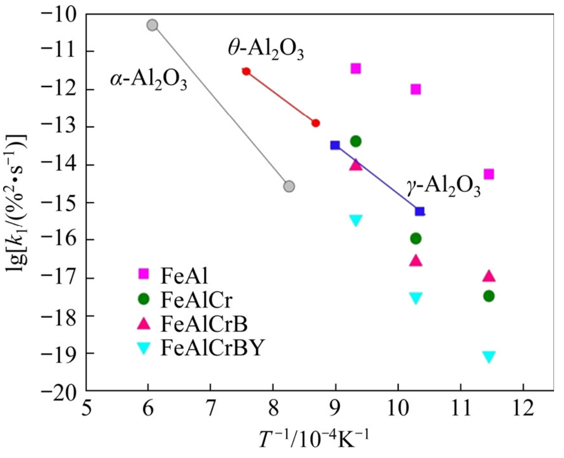

Fig. 4 Arrhenius diagram for porous FeAl, FeAlCr, FeAlCrB, and FeAlCrBY materials during oxidation

3.3 Changes of pore parameters

Pore size and open porosity are the prime parameters of filter materials, which need to be evaluated during high-temperature oxidation. Figure 5 shows the changes of the mean pore size and open porosity of these materials oxidized at 800 °C. With the duration of oxidation, the mean pore size of these materials decreases gradually. After 100 h of oxidation, the pore sizes of porous FeAl, FeAlCr, FeAlCrB, and FeAlCrBY decrease to 88.15%, 89.85%, 90.13%, and 90.28% of initial values, respectively, and the change ratio of open porosity varies from 24.94% to 6.92%. Obviously, with the sequential introduction of Cr, B, and Y, porous FeAl-based materials show the promotional resistance to oxidation.

3.4 Oxide-scale configuration formed at 800 °C

The oxidation kinetics and long-term structural stability of porous materials during oxidation often depend on the configuration of the oxide scales. Therefore, the oxide-scale configuration needs to be investigated comprehensively. Figure 6 shows the XRD patterns of these oxidized materials. After oxidation at 800 °C for 100 h, α-Al_2O_3 phase can be observed in all samples. Meanwhile, weak peaks of metastable γ-Al_2O_3 and θ-Al_2O_3 can be found on the

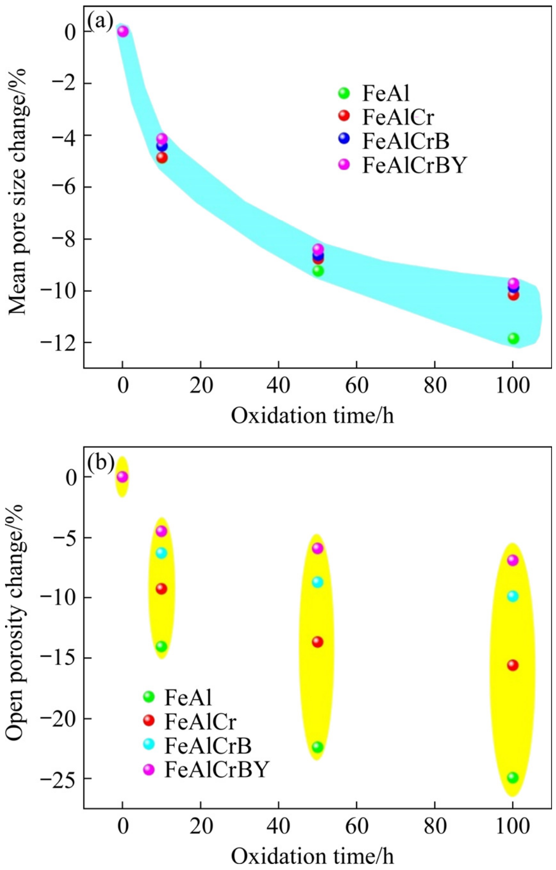

Fig. 5 Changes of mean pore size (a) and open porosity (b) of synthesized porous FeAl, FeAlCr, FeAlCrB, and FeAlCrBY materials as function of oxidation time at 800 °C

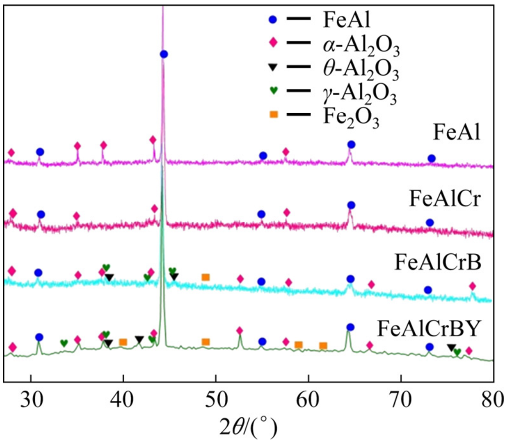

Fig. 6 XRD patterns of porous FeAl, FeAlCr, FeAlCrB, and FeAlCrBY materials after oxidation at 800 °C for 100 h

curves of porous FeAl and FeAlCr, but cannot be indexed in porous FeAlCrB and FeAlCrBY. This suggests that the alloying of B or B/Y probably restrains the formation of γ-Al_2O_3 and θ-Al_2O_3, or facilitates the growth of α-Al_2O_3. Fe_2O_3 is only detected in porous FeAl. The diffraction peaks of chromic oxides are usually superposed with those of Al_2O_3 and Fe_2O_3, and thus cannot be identified directly on the XRD patterns. Accordingly, it can be speculated that the enhanced oxidation resistance of porous FeAlCrBY is due to the preferential growth of α-Al_2O_3 and the restraint of less protective Fe_2O_3, γ-Al_2O_3, and θ-Al_2O_3.

The XPS was carried out to analyze the compositional and chemical states of superficial oxide scales. As shown in Table 4, the surface of these samples appears to be enriched in Al compared to the bulk composition. With the further addition of reactive elements (Cr/B/Y), the contents of Fe and Cr in the superficial layers of oxide scales decrease, while Al content increases. It is noteworthy that the contents of B and Y elements obtained by XPS are much higher than the nominal compositions, which indicates that B and Y elements may be enriched on the surface layers of oxidized porous FeAlCrB and FeAlCrBY samples. Figure 7 shows the 2p core levels of Al, Cr, and Fe for these materials. The Al 2p peaks with typical values of 73.7−74.1 eV are identified as various forms of Al_2O_3 [28]. The Fe $2p_{3/2}$ XPS spectra of the materials are found at 711.1−712.3 eV [29]. The Cr 2p spectra can be divided into 4 peaks, 576.8, 579.2, 585.1 and 588.0 eV, corresponding to Cr_2O_3, CrO_3, $FeCr_2O_4$ and $FeCr_2O_7$, respectively [29]. Therefore, the oxide scales of porous FeAl are mainly made up of Al_2O_3 and Fe_2O_3 (Fig. 7(a)), while in the oxidized porous FeAlCr (Fig. 7(b)) and FeAlCrB (Fig. 7(c)), the dissolved $FeCr_2O_4$ and $FeCr_2O_7$ oxides can be detected. An additional Al_2O_3 shoulder peak with large shifts of 2.6−2.8 eV is observed in the oxidized porous FeAlCrB and FeAlCrBY samples. Such phenomenon, usually observed in the initial stages of oxidation of the Al (111) surface [30], indicates that the selective

Table 4 Surficial chemical compositions (wt.%) of porous FeAl, FeAlCr, FeAlCrB, and FeAlCrBY materials after oxidation at 800 °C for 100 h by XPS analysis

Material	Fe	Al	Cr	B	Y	O
FeAl	1.7	37	−	−	−	61.3
FeAlCr	1.5	37.6	1.6	−	−	59.3
FeAlCrB	0.8	38.4	1.24	1.86	−	57.7
FeAlCrBY	0.2	43.3	0.2	0.9	0.3	55.1

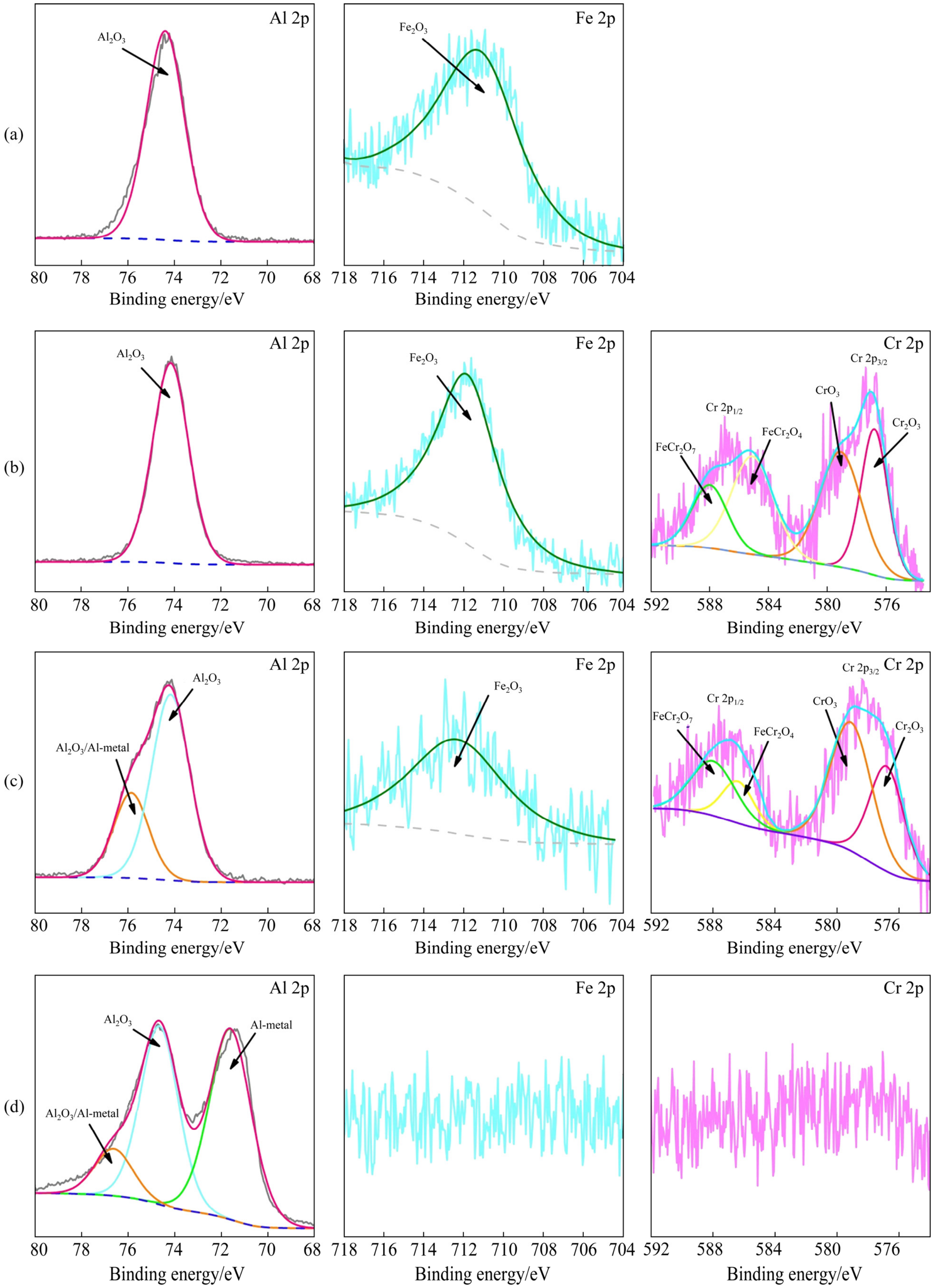

Fig. 7 Detailed XPS spectra of Al 2p, Fe 2p and Cr 2p of porous FeAl (a), FeAlCr (b), FeAlCrB (c), and FeAlCrBY (d) oxidized at 800 °C for 100 h

oxidation of Al and the preferred growth of Al_2O_3 may occur during the oxidation of porous FeAlCrB and FeAlCrBY. Interestingly, an intensive Al metallic peak (Al^0) is also found on the Al spectrum of porous FeAlCrBY, while the Fe 2p and Cr 2p spectra only show a poor signal-to-noise ratio, suggesting that these signals are not from the exposed zones where the protective oxide scale is partially peeled off during the cooling stages. Given the XRD analysis result, at least the superficial layer of oxide scales mainly consists of α-Al_2O_3.

Figure 8 shows the surface morphologies of these oxidized materials. The skeleton of porous FeAl is covered with oxides and has a rough appearance. Some "whisker-like" oxides [10] grow epitaxially toward the skeleton surface, as marked in Fig. 8(a). The evolution of the surface morphology of porous FeAl is shown in Fig. S1. After oxidation for 10 h, a fine equiaxed microstructure is observed, indicating that Fe and Al are synchronously oxidized. The surface of the sample oxidized for 50 h shows a "cabbage-like" structure, probably formed by the sintering of mixed Fe oxides and platelet γ-Al_2O_3 precursors [10]. It is suggested that the platelets are the results of an outward diffusion and oxidation of Al across the Fe-oxide grain boundaries [31]. In the sample of FeAl oxidized for 100 h, the sintering of the

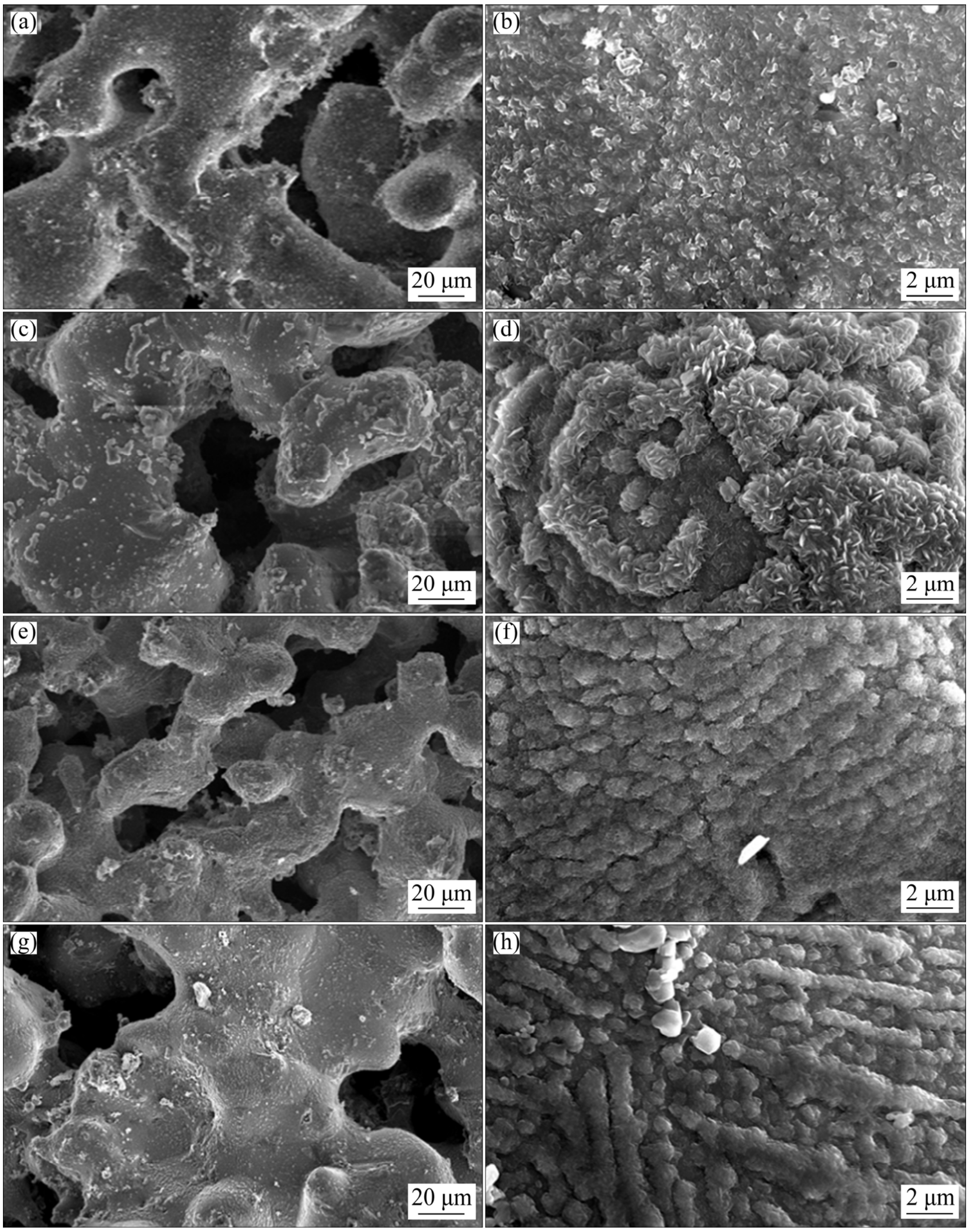

Fig. 8 SEM images of porous FeAl (a, b), FeAlCr (c, d), FeAlCrB (e, f), and FeAlCrBY (g, h) materials oxidized at 800 °C for 100 h

"cabbage-like" oxides is further developed, and some platelet-shaped oxide crystals can still be observed (Fig. 8(b)). According to the XRD retrieval, the oxide scales of porous FeAl are actually composed of defective Fe_2O_3, γ-Al_2O_3, and θ-Al_2O_3, which explains the high oxidation kinetic of porous FeAl.

Porous FeAlCr after 10 h oxidation also shows overall flat oxide scales on the surface of the porous framework (Fig. S2(a)). However, some oxide protrusions appear in some regions where the contents of Al and O are higher than those in flat regions, indicating the outward diffusion and oxidation of Al. The flaky characteristics of the oxides suggest these oxides can be the nucleated γ-Al_2O_3 [10] (Fig. S2(b)). After 50 h, these oxide platelets occupy nearly the entire surface of the porous skeleton (Fig. S2(c)). After 100 h oxidation, although porous FeAlCr gains less oxidation mass increment compared with porous FeAl, the integrity of the oxide scales is poor and the peeling occurs extensively on the porous skeleton surface (Fig. 8(c)). At higher magnification (Fig. 8(d)), it is seen that the oxide platelets increase in size with oxidation time. EDS analysis (Table S1) reveals that these platelet-like crystals are composed of Al, O as well as trace Fe and Cr. The regions of oxide scales peeled off display the relatively higher contents of Fe and Cr, showing a duplex oxide-scale structure with the compact inner layer and the supercrust platelets. These observations are in good agreement with those reported by KADIRI et al [10]. In the Fe−Cr−Al system, it has been confirmed that the presence of Cr can produce the Cr-induced Al-pump [17], accelerating the outward diffusion of Al and the preferential formation of Al_2O_3 scales. However, the outer Al_2O_3 scales comprosed of highly defected plate-like γ-Al_2O_3 provide limited resistance to oxidation. The improved antioxidation property of porous FeAlCr should be the result of the inner dense layer of oxide scales.

The morphologies of oxide scales formed on porous FeAlCrB and FeAlCrBY skeletons at 800 °C are quite different from those on porous FeAl and FeAlCr. The oxide scales of these two materials consist of nodular oxides (Figs. S3 and S4) [17]. In the initial oxidation process, nodular oxides, with higher Al content than the nearby flat oxidized region (Tables S2 and S3), grow epitaxially on the surfaces of porous FeAlCrB and FeAlCrBY skeletons. As oxidation proceeds, these nodular oxides increase both in size and number. After oxidation for 50 h, the nodular oxides are predominant. The composition analysis shows that the proportion of Al element in both nodular and flat regions is also improved. Furthermore, the contents of Fe and Cr in the Al-rich oxide scales of porous FeAlCrBY are lower than those of porous FeAlCrB, which agrees with the XPS analysis results.

As shown in Figs. 8(e, f), after oxidation for 100 h, the overlying oxide scales on porous FeAlCrB skeleton are dense and integral. The oxide scales are made up of nodular oxides adjacent to each other. However, some micro-cracks can be found among the nodular oxides (Fig. 8(f)), which can be attributed to the growing stress of thickened oxide scales during cooling stage or volatilization of boron oxides at high temperature [32,33]. Figures 8(g, h) show that the distribution density of nodular oxides and the thickness of the oxide scales of porous FeAlCrBY are lower than those of porous FeAlCrB, indicating the lower oxidation kinetics and the effective role of reactive element Y.

These isostructural nodular oxides are verified as α-Al_2O_3 by XRD (Fig. 6). Some researches reported that Fe-oxide nodules formed at the initial stage of oxidation can serve as crystallographic templates for the subsequent oxides [10,11,17]. When considering the evolution of oxide-scale morphologies of porous FeAlCrB and FeAlCrBY, it is speculated that the corundum-structure Al_2O_3 should be directly generated rather than transformed from the metastable oxide phases. Some research [14,34] also revealed that α-Al_2O_3 could be formed at the interface between the metal and oxide scales at relatively low temperatures after the formation of continuous covering oxide scales, benefitting from the reduced oxygen partial pressure and the crystallographic template effect of α-Fe_2O_3 or α-Cr_2O_3. Obviously, the formation of protective α-Al_2O_3 scales on porous FeAlCrB and FeAlCrBY is mainly due to the introduction of B. Meanwhile, coalloying of B and Y further modifies the integrity of α-Al_2O_3 oxide scales via eliminating the micro-cracks between nodular oxides, which can account for the reduced oxidation rate of porous FeAlCrBY.

3.5 Roles of B and Y

Figure 9 shows the element distributions of the four oxidized materials along the thickness direction. With the introduction of Cr, B, and Y, the thickness of the oxide scales decreases from about 2.0 to 1.0 μm, which corresponds to the mass gain results. The oxide scales of these materials can all be partitioned into the inner layer composed of Al, Cr, and Fe oxides and the outer layer mainly composed of Al_2O_3 with a trace amount of Fe or Fe/Cr oxides. With the addition of reactive elements (Figs. 9(b−d), the contents of the doped Fe or Fe/Cr in the Al_2O_3 scales of porous FeAlCrB and FeAlCrBY are significantly reduced, consistent with the XPS (Fig. 7) and EDS (Tables S1, S2 and S3) analysis results. This suggests that the formation of less defective external Al_2O_3 scales protects the gracile porous skeleton against oxidation.

Moreover, it is noted that B is enriched on the surface of oxide scales of porous FeAlCrB (Fig. 9(c)), indicating that during oxidation boron diffuses from the bulk to the surface and participates in the formation of oxide scales. In FeAl-based alloys, boron tends to segregate in and strongly interact with the grain boundary, vacancy, dislocation, and other defects to reduce the diffusion of alloying elements [35]. During oxidation, the contents of Fe, Cr, and Al are much higher than the content of B, so the in-situ oxidation of Fe, Cr, and Al at the initial stage is inevitable. In general, the outward transport of Al to the surface is mainly accomplished by the vacancy mechanism [36]. Meanwhile, above 800 °C, the diffusion rate of B is faster than that of vacancies. Hence, an enriched layer of boron can be formed on the surface of porous FeAlCrB or FeAlCrBY, which hinders the absorption of oxygen atoms and sharply reduces the oxygen partial pressure. Thus, the proliferation of Fe/Cr oxides is difficult and only Al with stronger oxygen-binding ability can be oxidized. As a result, the external oxide layers of porous FeAlCrB or FeAlCrBY samples are almost single alumina layers.

In Fig. 9(d), it is seen that Y is enriched on the interface of the inner layer and outer layer, which accords with a theoretical study [37] which states that due to the large ionic radius of yttrium compared with that of aluminum ions, yttrium ions are located at the scale−metal interface and can block cation vacancy diffusion in the scale. Compared with Y-free alloys, yttrium alloying can suppress the outward lattice transport of aluminum ions through the scale and allow inwardly transporting oxygen to reach the scale metal interface via the grain boundaries of α-Al_2O_3 scales. Thus, less stress is produced in oxide scales and the adhesivity of oxide scales to the substrate can be increased, which contributes to the reduced oxidation rate.

Table 5 summarizes the phase compositions of the oxide scales of a series of FeAl-based alloys during oxidation at high temperatures. Whether for FeAl, FeCrAl alloys or FeAlCr alloys with the minor additions of various reactive elements such as Zr, B, Y, Ti, and Si, the single α-Al_2O_3 scales are

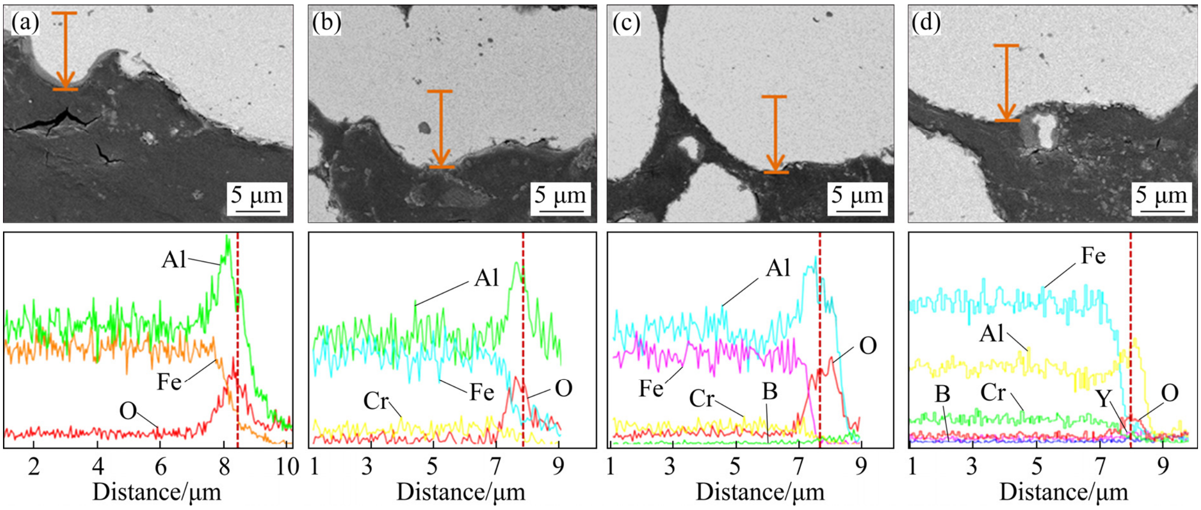

Fig. 9 Element distributions along EDS scanning line based on cross-sections of porous FeAl (a), FeAlCr (b), FeAlCrB (c) and FeAlCrBY (d) materials oxidized at 800 °C for 100 h

Table 5 Comparison of phase compositions of oxide scales of FeAl-based alloys during oxidation at high temperatures

Alloy composition	Oxidation temperature/°C	Phases of oxides	Ref.
*B*2-FeAl	900	θ-Al_2O_3, α-Al_2O_3	[38]
	1000	α-Al_2O_3	
*B*2-ODS FeAl	950	θ-Al_2O_3, α-Al_2O_3	[38]
	1000	α-Al_2O_3	
Fe−15Cr−10Al, Fe−13Cr−17Al, Fe−11Cr−25Al, Fe−7Cr−40Al (at.%)	1100	α-Al_2O_3	[39]
Fe−25.27Al−5.48Cr−0.068Zr−0.012B (wt.%)	800	θ-Al_2O_3, γ-Al_2O_3	[8]
	900	γ-Al_2O_3, θ-Al_2O_3, α-Al_2O_3	
	1000	α-Al_2O_3	
Fe−21.3Cr−5.1Al−0.08Ti−0.03Y−0.06Zr−0.3Si−0.03C−0.01Mg (wt.%)	900	α-Al_2O_3, γ-Al_2O_3	[40]
Fe−10Cr−22.5Al−0.2B, Fe−10Cr−22.5Al−0.2B−0.2Y (wt.%)	800	α-Al_2O_3	This work

only found at oxidation temperatures above 1000 °C [8,38−40]. In this study, with the aid of relatively high contents of Cr, B, and Y, porous FeAl intermetallics can produce single α-Al_2O_3 oxide scales when oxidized at about 800 °C in air.

4 Conclusions

(1) Alloying elements Cr, B, and Y were introduced into the synthesis of porous *B*2-structured FeAl intermetallics after sintering these alloying elements are well dissolved in FeAl phase. The addition of Cr, B, and Y to the Fe−Al binary alloy also facilitates the pore forming process.

(2) The oxidation mass gain of porous FeAl alloyed with Cr, B, and Y can be reduced to 0.39% after being oxidized at 800 °C for 100 h. Porous FeAlCrBY shows a preferable pore-structure stability and resistance against high-temperature oxidation.

(3) The nodular α-Al_2O_3 oxide scales are formed on the 800 °C-oxidized porous FeAlCrB, while the coalloying of B and Y further modifies the integrity of α-Al_2O_3 oxide scales via eliminating the micro-cracks.

(4) The oxide scales of porous FeAlCrBY have a duplex structure. B is enriched on the surface of oxide scales and Y is located at the scale−metal interface. The coalloying of B and Y promotes the formation of thin protective alumina layer.

Acknowledgments

The authors are grateful for the financial supports from the National Natural Science Foundation of China (No. 51801183) and the Natural Science Foundation of Zhejiang Province, China (No. GG21E010011).

Supporting materials

Supporting materials in this work can be found at: http://www.ysxbcn.com/download/13-p2620-2021-0784-supporting-materials.pdf

References

[1] HEIDENREICH S. Hot gas filtration—A review [J]. Fuel, 2013, 104: 83−94. https://doi.org/ 10.1016/j.fuel.2012.07.059.

[2] CÓRDOBA P. Status of flue gas desulphurisation (FGD) systems from coal-fired power plants: Overview of the physic-chemical control processes of wet limestone FGDs [J]. Fuel, 2015, 144: 274−286. https://doi.org/10.1016/j.fuel.2014.12.065.

[3] ZHANG H B, LIU X L, JIANG Y, GAO L, YU L P, LIN N, HE Y H, LIU C T. Direct separation of arsenic and antimony oxides by high-temperature filtration with porous FeAl intermetallic [J]. Journal of Hazardous Materials, 2017, 338: 364−371. https://doi.org/ 10.1016/j.jhazmat.2017.05.049.

[4] ZHANG H B, XIE W, GAO H Y, SHEN W J, HE Y H. Suppression of the SHS reactions during synthesis of porous FeAl intermetallics by introducing silicon [J]. Journal of Alloys and Compounds, 2018, 735: 1435−1438. https://doi.org/ 10.1016/j.jallcom.2017.11.291.

[5] GAO H J, XIE W, ZHANG H B, SHEN W J, HE Y H. Modification of the reactive synthesis of porous FeAl with addition of Si [J]. Materials at High Temperatures, 2019, 36:

1−8. https:// doi.org/10.1080/09603409.2018.1439683.

[6] ZHANG H B, GAO H Y, LIU X L, YU H, WANG L F, JIANG Y, GAO L, YU L P, HE Y H, CHEN X M, ZHANG L, ZHENG G Q. Reactive synthesis and assessment of porous Fe−20.5Al−18Cr intermetallic material: A comparative study with porous FeCrAl material produced from prealloyed powders [J]. Separation and Purification Technology, 2019, 220: 152−161. https://doi.org/10.1016/j.seppur.2019.03.054.

[7] PALM M. Concepts derived from phase diagram studies for the strengthening of Fe−Al-based alloys [J]. Intermetallics, 2005, 13: 1286−1295. https://doi.org/ 10.1016/j.intermet.2004.10.015.

[8] NOWAK K, KUPKA M. High-temperature oxidation behaviour of B2 FeAl based alloy with Cr, Zr and B additions [J]. Materials Chemistry and Physics, 2012, 132: 902−908. https://doi.org/10.1016/j.matchemphys.2011.12.031.

[9] STOTT F H, WOOD G C, STRINGER J. The influence of alloying elements on the development and maintenance of protective scales [J]. Oxidation of Metals, 1995, 44: 113−145. https://doi.org/ 10.1007/BF01046725.

[10] KADIRI H E, MOLINS R, BIENVENU Y, HORSTEMEYER M F. Abnormal high growth rates of metastable aluminas on FeCrAl alloys [J]. Oxidation of Metals, 2005, 64: 63−97. https://doi.org/10.1007/s11085-005-5715-0.

[11] BRITO P, PINTO H, KOSTKA A. The crystallographic template effect assisting the formation of stable α-Al_2O_3 during low temperature oxidation of Fe−Al alloys [J]. Corrosion Science, 2016, 105: 100−108. https://doi.org/10.1016/j.corsci.2016.01.007.

[12] BAI Y P, XING J D, GUO Y C, LI J P, HE Y Y, MA S Q. Effect of Cr on microstructure, mechanical properties, and wear behavior of in situ 20 wt.%Al_2O_3/Fe−25Al composites [J]. Journal of Materials Engineering and Performance, 2015, 24: 936−945. https://doi.org/ 10.1007/s11665-014-1367-z.

[13] VIGUIER B, MARTINEZ M, LACAZE J. Characterization of complex planar faults in FeAl(B) alloys [J]. Intermetallics, 2017, 83: 64−69. https://doi.org/10.1016/j.intermet.2016.12.005.

[14] YOUNG D J, NAUMENKO D, NIEWOLAK L, WESSEL E, SINGHEISER L, QUADAKKERS W J. Oxidation kinetics of Y-doped FeCrAl alloys in low and high pO_2 gases [J]. Materials and Corrosion, 2010, 61: 838−844. https://doi.org/10.1002/maco.200905432.

[15] HUANG C, ZHANG P Z, WEI D B, WEI X F, CHEN X H, DING F. Tribological behaviour of double-glow plasma zirconium- yttrium alloying on γ-TiAl [J]. Surface Engineering, 2017, 33(12): 911−918. https://doi.org/10.1080/02670844.2016. 1266745.

[16] PAN D, ZHANG R Q, WANG H, LU C, LIU Y M. Formation and stability of oxide layer in FeCrAl fuel cladding material under high-temperature steam [J]. Journal of Alloys and Compounds, 2016, 684: 549−555. https://doi.org/10.1016/j. jallcom.2016.05.145.

[17] AIRISKALLIO E, NURMI E, HEINONEN M H, VÄYRYNEN I J, KOKKO K, ROPO M, PUNKKINEN M P J, PITKÄNEN H, ALATALO M, KOLLÁR J, JOHANSSON B, VITOS L. High temperature oxidation of Fe−Al and Fe−Cr−Al alloys: The role of Cr as a chemically active element [J]. Corrosion Science, 2010, 52: 3394−3404. https://doi.org/ 10.1016/j.corsci.2010.06.019.

[18] LIU X, GLEESON B. The effect of environmental sulfur on the establishment and structural stability of alumina scales [J]. Oxidation of Metals, 2013, 80: 517−527. https://doi.org/10.1007/s11085-013-9444-5.

[19] GLASSCOCK J A, MIKKELSEN L, PERSSON Å H, PEĆANAC G, MALZBENDER J, BLENNOW P, BOZZA F, HENDRIKSEN P V. Porous Fe21Cr7Al1Mo0.5Y metal supports for oxygen transport membranes: Thermo-mechanical properties, sintering and corrosion behavior [J]. Solid State Ionics, 2013, 242: 33−44. https://doi.org/10.1016/j.ssi.2013.04.006.

[20] HERNÁNDEZ A, CALVO J I, PRÁDANOS P, TEJERINA F. Pore size distributions in microporous membranes: A critical analysis of the bubble point extended method [J]. Journal of Membrane Science, 1996, 112: 1−12. https://doi.org/10.1016/0376-7388(95)00025-9.

[21] ZHANG H B, GAO H Y, YU H, WANG L F, LIU X L, MA J L, ZHANG N H, HE Y H, JIANG Y. The role of Cr in the reactive synthesis of porous FeAlCr intermetallic compounds [J]. Materials Chemistry and Physics, 2020, 249: 123013. https://doi.org/ 10.1016/j.matchemphys.2020.123013.

[22] JIANG Yao, HE Yue-hui, GAO Hai-yan. Pore constitution and tortuosity factor of reactively synthesized porous TiAl intermetallic compound [J]. Transactions of Nonferrous Metals Society of China, 2021, 31: 726−733. https://doi.org/10.1016/S1003-6326(21)65533-4.

[23] BRADY M P, WRIGHT I G, GLEESON B. Alloy design strategies for promoting protective oxide-scale formation [J]. JOM, 2000, 52: 16−21. https://doi.org/10.1007/s11837-000-0109-x.

[24] MOLIN S, KUSZ B, GAZDA M, JASINSKI P. Evaluation of porous 430L stainless steel for SOFC operation at intermediate temperatures [J]. Journal of Power Sources, 2008, 181: 31−37. https://doi.org/10.1016/j.jpowsour.2007.10.009.

[25] MOLIN S, GAZDA M, KUSZ B, JASINSKI P. Evaluation of 316L porous stainless steel for SOFC support [J]. Journal of the European Ceramic Society, 2009, 29: 757−762. https://doi.org/ 10.1016/j.jeurceramsoc.2008.07.027.

[26] SARASKETA-ZABALA E, OTAEGI L, RODRIGUEZ-MARTINEZ L M, ALVAREZ M A, BURGOS N, CASTRO F, VILLARREAL I. High temperature stability of porous metal substrates under highly humidified hydrogen conditions for metal supported solid oxide fuel cells [J]. Solid State Ionics, 2012, 222: 16−22. https://doi.org/10.1016/j.ssi.2012.06.014.

[27] JOSEFSSON H, LIU F, SVENSSON J E, HALVARSSON M, JOHANSSON L G. Oxidation of FeCrAl alloys at 500−900 °C in dry O_2 [J]. Materials and Corrosion, 2005, 56: 801−805. https://doi.org/ 10.1002/maco.200503882.

[28] ALEXANDER M R, THOMPSON G E, BEAMSON G. Characterization of the oxide/hydroxide surface of aluminium using X-ray photoelectron spectroscopy: a procedure for curve fitting the O1s core level [J]. Surface and Interface Analysis, 2000, 29: 468−477. https://doi.org/10.1002/1096-9918(200007)29.

[29] CHEN G, WANG H, SUN H Y, ZHANG Y Y, CAO P, WANG J. Effects of Nb-doping on the mechanical properties and high-temperature steam oxidation of annealing FeCrAl fuel cladding alloys [J]. Materials Science & Engineering A, 2021, 803: 140500. https://doi.org/10.1016/j.msea.2020.140500.

[30] PARLE J K, BENI A, DHANAK V R, SMERDON J A, SCHMUTZ P, WARDÉ M, BARTHÉS-LABROUSSE M G, BAUER B, GILLE P, SHARMA H R, MCGRATH R. STM and XPS investigation of the oxidation of the Al_4(Cr,Fe) quasicrystal approximant [J]. Applied Surface Science, 2013, 283: 276−282. https://doi.org/ 10.1016/j.apsusc.2013.06.101.

[31] JEDLINSKI J, GLAZKOV A, KONOPKA M, BORCHARDT G, TSCHERKASOVA E, BRONFIN M, NOCUŃ M. An XPS/SEM/EDX study of the early oxidation stages of the Fe19Cr5Al(+Y) alumina-forming alloys [J]. Applied Surface Science, 1996, 103: 205−216. https://doi.org/10.1016/0169- 4332(96)00521-1.

[32] LI Tie-fan. High temperature oxidation and hot corrosion of metals [M]. Chemical Industry Press, Beijing, 2003: 39−51. (in Chinese)

[33] FAN J X, HU X J, BAO B H, CHENG L. Effect of trace boron on oxide layer structure of Fe−Cr−Al alloy at high temperature [J]. Heat Treatment of Metals, 2017, 42: 77−81. (in Chinese)

[34] ZHANG X J, WANG S Y, GESMUNDO F, NIU Y. The effect of Cr on the oxidation of Ni−10at.%Al in 1 atm O_2 at 900−1000 °C [J]. Oxidation of Metals, 2006, 65: 151−165. https://doi.org/ 10.1007/s11085-006-9009-y.

[35] KIM S I, CHOI S H, LEE Y. Influence of phosphorous and boron on dynamic recrystallization and microstructures of hot-rolled interstitial free steel [J]. Materials Science & Engineering A, 2005, 406: 125−133. https://doi.org/10.1016/j.msea.2005.06.040.

[36] ZHANG G Y, ZHANG H, FANG G L, LUO Z C. Electronic theoretical study of the mechanism of the oxide scale formation of Fe−Cr−Al alloy [J]. Acta Physica Sinica, 2009, 8: 6441−6445. https://doi.org/10.3321/j.issn:1000-3290.2009.09.091.

[37] ANDERSON A B, MEHANDRU S P, SMIALEK J L. Dopant effect of yttrium and the growth and adherence of alumina on nickel-aluminum alloys [J]. Journal of the Electrochemical Society, 1985, 132: 1695−1701. https://doi.org/ 10.1149/1.2114193.

[38] CHAN C D N, HUVIER C, DINHUT J F. High temperature corrosion of some *B*2 iron aluminides [J]. Intermetallics, 2001, 9: 817−826. https://doi.org/ 10.1016/S0966-9795(01)00065-6.

[39] SHMORGUN V G, BOGDANOV A I, KULEVICH V P. The effect of aluminum content in the Fe−Cr−Al system alloys on the oxide films phase composition [J]. Materials Today−Proceedings, 2020, 30: 554−558. https://doi.org/10.1016/j.matpr.2020.01.133.

[40] FANG L, TLIND H G, SVENSSON J E, JOHANSSON L G, HALVARSSON M. Early stages of the oxidation of a FeCrAlRE alloy (Kanthal AF) at 900 °C: A detailed microstructural investigation [J]. Corrosion Science, 2008, 50: 2272−2281. https://doi.org/10.1016/j.corsci.2008.05.019.

高硼/钇合金化提高 FeAl 基金属间化合物多孔材料的抗氧化性能

张惠斌，余 航，马俊良，王龙飞，徐圣航，郑国渠

浙江工业大学 材料科学与工程学院，杭州 310014

摘 要：利用反应合成法制备高铬(Cr)、硼(B)、钇(Y)复合合金化的 *B*2 结构 FeAl 基金属间化合物多孔材料，通过研究 FeAl 基多孔材料氧化后的孔结构演变、氧化动力学和氧化膜构型，探讨其高温氧化行为。结果显示，添加高含量合金元素 Cr、B 和 Y 后，FeAl 多孔材料在 600~800 ℃下氧化增质显著降低。富集在氧化膜表面的 B 和偏聚在氧化膜与基体界面处的 Y 共同促进多孔材料表面形成薄且具有优异防护性的结节状 α-Al_2O_3 氧化膜。研究表明，引入较高含量的活性元素如 B 和 Y 有利于 FeAl 金属间化合物在较低氧化温度和无预处理的情况下选择性生长单一的 α-Al_2O_3 氧化膜。

关键词：FeAl；金属间化合物；钇；高温滤材；氧化；多孔材料

(Edited by Bing YANG)